

# Copper(II)-bis-Histidine Coordination Structure in a Fibrillar Amyloid $\beta$ -Peptide Fragment and Model Complexes Revealed by Electron Spin Echo Envelope Modulation Spectroscopy

Jessica Hernández-Guzmán,<sup>[a]</sup> Li Sun,<sup>[a]</sup> Anil K. Mehta,<sup>[b]</sup> Jijun Dong,<sup>[b]</sup> David G. Lynn,<sup>[b]</sup> and Kurt Warncke<sup>\*[a]</sup>

Truncated and mutated amyloid- $\beta$  (A $\beta$ ) peptides are models for systematic study—in homogeneous preparations—of the molecular origins of metal ion effects on A $\beta$  aggregation rates, types of aggregate structures formed, and cytotoxicity. The 3D geometry of bis-histidine imidazole coordination of Cu<sup>II</sup> in fibrils of the nonapeptide acetyl-A $\beta$ (13–21)H14A has been determined by powder <sup>14</sup>N electron spin echo envelope modulation (ESEEM) spectroscopy. The method of simulation of the anisotropic combination modulation is described and benchmarked for a Cu<sup>II</sup>-bis-*cis*-imidazole complex of known structure. The re-

vealed bis-*cis* coordination mode, and the mutual orientation of the imidazole rings, for Cu<sup>II</sup> in Ac-A $\beta$ (13–21)H14A fibrils are consistent with the proposed  $\beta$ -sheet structural model and pairwise peptide interaction with Cu<sup>II</sup>, with an alternating [–metal-vacancy–]<sub>n</sub> pattern, along the N-terminal edge. Metal coordination does not significantly distort the intra- $\beta$ -strand peptide interactions, which provides a possible explanation for the acceleration of Ac-A $\beta$ (13–21)H14A fibrillization by Cu<sup>II</sup>, through stabilization of the associated state and low-reorganization integration of  $\beta$ -strand peptide pair precursors.

## Introduction

Alzheimer's disease (AD) afflicts over 25 million people, is among the top ten leading causes of death worldwide, and is the number one cause of dementia.<sup>[1,2]</sup> A morphological hallmark of AD is the accumulation of the amyloid  $\beta$ -protein [A $\beta$ ; native peptides are  $n$  = 39–43 residues in length and are denoted A $\beta$ (1– $n$ )] in plaques and neurofibrillary tangles in the human brain.<sup>[3]</sup> The divalent metal ions Zn<sup>II</sup> and Cu<sup>II</sup> have been found at elevated concentrations ( $>10^{-4}$  M) in Alzheimer's plaques,<sup>[4–8]</sup> and the association of A $\beta$  with metal ions has been correlated with AD.<sup>[4,9,10]</sup> Metal ions have also been shown to be correlated with amyloid aggregation in the neurodegenerative prion<sup>[11–13]</sup> and Parkinson's diseases.<sup>[14,15]</sup>

Electron spin echo envelope modulation (ESEEM)<sup>[16–18]</sup> and hyperfine sublevel correlation (HYSCORE)<sup>[19]</sup> spectroscopies have implicated the three histidine (H) residues H6, H13, and H14 in the N-terminal domain of A $\beta$  in Cu<sup>II</sup> binding, and have elucidated the coordination structure in the soluble A $\beta$ (1–


16)<sup>[20–25]</sup> and A $\beta$ (1–28)<sup>[26–28]</sup> peptides. Solid-state nuclear magnetic resonance (SS-NMR)<sup>[8]</sup> and ESEEM<sup>[29]</sup> spectroscopies have addressed the Cu<sup>II</sup> coordination structure in the fibrillar form of full-length A $\beta$ (1–40). The ESEEM study identified bis-*cis*-H-imidazole coordination at two distinct sites and led to a structural model in which Cu<sup>II</sup>-H6/H13 and Cu<sup>II</sup>-H6/H14 sites alternate along the fibril axis, on opposite sides of the  $\beta$ -sheet fibril structure.<sup>[29]</sup>

Truncated and mutated A $\beta$  peptides allow systematic study—in homogeneous preparations—of the molecular basis of the effects of metal ions on rates of A $\beta$  aggregation, types of aggregate structures formed, and cytotoxicity.<sup>[30]</sup> Insights into metal ion control of amyloid structure are also valuable for manipulating modified A $\beta$  peptides, for forming nanomaterial scaffolds, for templating ordered molecular arrays,<sup>[31–33]</sup> or for metal deposition,<sup>[34,35]</sup> to create energy- and charge-transfer functionalities.

The truncated and N-terminal-acetylated A $\beta$  nonapeptide Ac-HHQLVFFA [Ac-A $\beta$ (13–21)] contains the core hydrophobic segment A $\beta$ (17–21), which is necessary for fibrillization,<sup>[31,36,37]</sup> and the metal-binding dyad H14–H15.<sup>[38]</sup> The Ac-A $\beta$ (13–21)H14A mutant nonapeptide forms homogeneous fibrils in the presence of Cu<sup>II</sup> and recapitulates the parallel, in-register  $\beta$ -sheet structure found in fibrillar forms of A $\beta$ (1–40)<sup>[39–41]</sup> and A $\beta$ (1–42).<sup>[42]</sup> Cu<sup>II</sup>-Ac-A $\beta$ (13–21)H14A also displays cytotoxicity comparable to that of full-length A $\beta$ , whereas the apo-peptide is benign.<sup>[30]</sup> Fibrillization of Ac-A $\beta$ (13–21)H14A is accelerated by Cu<sup>II</sup>. A structure model for the Cu<sup>II</sup>-Ac-A $\beta$ (13–21)H14A fibril was proposed;<sup>[30]</sup> in this, Cu<sup>II</sup> is bis-coordinated by a histidine

[a] Dr. J. Hernández-Guzmán, Dr. L. Sun, Prof. K. Warncke  
Department of Physics, Emory University  
Atlanta, GA 30322-2430 (USA)  
E-mail: kwarncke@physics.emory.edu

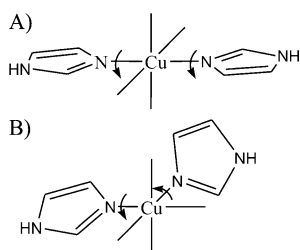
[b] Dr. A. K. Mehta, Dr. J. Dong, Prof. D. G. Lynn  
Department of Chemistry, Emory University  
Atlanta, GA 30322-2430 (USA)

 Supporting information for this article is available on the WWW under <http://dx.doi.org/10.1002/cbic.201300236>: stereoplot of the physical model for the Cu<sup>II</sup>(2-Melm)<sub>2</sub>(OAc)<sub>2</sub> complex, depiction of rotations that reorient the two remote <sup>14</sup>N shf PAS in [Cu<sup>II</sup>(2-Melm)<sub>2</sub>(OAc)<sub>2</sub>] in the physical model derived from ESEEM, calculated physical model for the Cu<sup>II</sup>-bis-trans-imidazole complex Cu<sup>II</sup>(him)<sub>2</sub>(NO<sub>3</sub>)<sub>2</sub>.

imidazole ligand from each of two peptides, in an arrangement that extends along the fibril axis as follows: (–peptide–Cu<sup>II</sup>–peptide–peptide–Cu<sup>II</sup>–peptide–)<sub>n</sub>.

In contrast with the interaction of Cu<sup>II</sup> with Ac-Aβ(13–21)H14A, interaction of Cu<sup>II</sup> with the peptide Aβ(13–21)K16A blocks the fibril formation characteristic of the apo-Aβ(13–21)K16A and leads to formation of a dipeptide complex that is not cytotoxic.<sup>[30]</sup> The Aβ(13–21)K16A peptide displays Cu<sup>II</sup>-mono-H equatorial coordination, whereas Ac-Aβ(13–21)H14A shows Cu<sup>II</sup>-bis-H equatorial coordination.<sup>[30]</sup> The Cu<sup>II</sup>-peptide coordination geometry is thus a critical determinant of the differences in peptide aggregation state, structure, and cytotoxicity.

We have developed an ESEEM spectroscopic approach for the determination of the mutual orientation of equatorial bis-imidazole ligands in Cu<sup>II</sup> complexes in disordered (powder) systems.<sup>[29,43]</sup> As depicted in Scheme 1, the method leads to speci-



**Scheme 1.** Depiction of the equatorial bis-*cis*- and bis-*trans*-imidazole coordination of Cu<sup>II</sup> and rotational degrees of freedom of the imidazole group. A) Cu<sup>II</sup>-bis-*trans*-imidazole. B) Cu<sup>II</sup>-bis-*cis*-imidazole.

fication of the bis-*cis* or bis-*trans* mode of coordination and the mutual orientation of the two imidazole rings. The <sup>14</sup>N ESEEM from the remote (non-coordinated) nitrogen nuclei of the H imidazole ligands is detected.<sup>[44]</sup> The ESEEM experiment is performed at an external magnetic field value that corresponds to the  $g_{\perp}$  position in the Cu<sup>II</sup> EPR line shape, at the quasi-powder position<sup>[45]</sup> of maximum transition intensity. This increases the detection sensitivity for the ESE at the low electron spin contents typical of Aβ protein samples. The analysis of the <sup>14</sup>N ESEEM focuses on modulation from the combinations of the anisotropic,  $\Delta m_{i\beta} = \pm 2$  modulation, from the pair of coupled <sup>14</sup>N nuclei. In the ESEEM spectrum, “combination lines” occur at sums of the fundamental <sup>14</sup>N coupling frequencies. The ligand geometry information is extracted from the mutual orientation of the <sup>14</sup>N dipolar super-hyperfine (shf) tensors.<sup>[29,43]</sup> The large parameter space of the numerical simulation of the ESEEM is efficiently searched for the global minimum by the hybrid optimization algorithm in the ESEEM simulation software package, known as OPTESIM.<sup>[43]</sup> OPTESIM also provides a statistical assessment (simultaneous confidence region) for each parameter.<sup>[43]</sup> The method has been validated by application to a Cu<sup>II</sup>-bis-*trans*-imidazole model complex of known structure<sup>[43]</sup>—Cu<sup>II</sup>-bis-histamine-bis-nitrate [Cu<sup>II</sup>(him)<sub>2</sub>(NO<sub>3</sub>)<sub>2</sub>]<sup>[46]</sup>—and used to determine the Cu<sup>II</sup> coordination structure in fibrillar Aβ(1–40).<sup>[29]</sup>

Here the method is benchmarked for Cu<sup>II</sup>-bis-*cis*-imidazole coordination, by using the complex Cu<sup>II</sup>-bis-(acetate)-bis-(2-methylimidazole) [Cu<sup>II</sup>(2-Melm)<sub>2</sub>(OAc)<sub>2</sub>]<sup>[54]</sup> of known structure. Application to Cu<sup>II</sup> coordination in Aβ(13–21)H14A fibrils reveals a bis-*cis*-imidazole coordination and the mutual geometry of the imidazole rings. This quantifies features of the Cu<sup>II</sup> site structure in Aβ(13–21)H14A fibrils, as well as defining structural constraints for accurate modeling of the peptide configuration and fibril conformation. The refined model for intra-β-sheet coordination of Cu<sup>II</sup> provides a possible explanation for acceleration of fibrillization by Cu<sup>II</sup>.

## Results

### EPR spectroscopy of Cu<sup>II</sup>-imidazole model complexes and Aβ peptides

Figure 1 shows the continuous-wave X-band powder EPR spectra of Cu<sup>II</sup>(dien)(2-Melm), Cu<sup>II</sup>(2-Melm)<sub>2</sub>(OAc)<sub>2</sub>, Cu<sup>II</sup>-Aβ(13–21)K16A, and Cu<sup>II</sup>-Aβ(13–21)H14A. The spectra are each characteristic of a square-planar Cu<sup>II</sup> complex and show resolved copper hyperfine splitting, which is centered at  $g_{\parallel}$ , from interaction of the unpaired electron spin with the  $I = 3/2$  copper nucleus.<sup>[45,47]</sup> The amplitudes of the powder EPR spectra are greatest around the  $g_{\perp} \approx 2$  region. This corresponds to the position of the external magnetic field of 3030 G that was used to achieve the maximum ESE amplitude in the ESEEM experiments. Each EPR spectrum in Figure 1 is consistent with a single spectral component. The EPR spectrum of Cu<sup>II</sup>-Aβ(13–

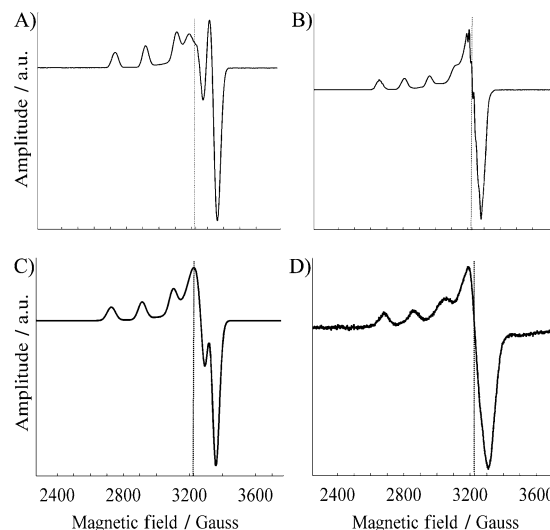


**Figure 1.** X-band continuous-wave EPR spectra of Cu<sup>II</sup>-imidazole model complexes and Aβ(13–21) complexes. A) [Cu<sup>II</sup>(dien)(2-Melm)]. B) [Cu<sup>II</sup>(2-Melm)<sub>2</sub>(OAc)<sub>2</sub>]. C) [Cu<sup>II</sup>-Aβ(13–21)K16A]. D) [Cu<sup>II</sup>-Aβ(13–21)H14A]. The lighter dashed vertical line in each case shows the position of the magnetic field that corresponds to the ESEEM collection, scaled for the different microwave frequencies used in the CW-EPR and ESEEM experiments. Conditions: microwave frequency 9.3411 GHz, microwave power 2 mW, microwave attenuation 20 dB, magnetic field modulation 1.5 G, modulation frequency 100 kHz, field sweep rate 1.5 G s<sup>−1</sup>, time constant 2.56 ms, temperature 120 K for model complexes and 165 K for Aβ(13–21) peptides, average of 12 sweeps minus average of 12 baseline spectra.

21)H14A displays a general broadening of the  $\text{Cu}^{\text{II}}$  hyperfine and  $g_{\perp} \approx 2$  features, relative to the molecular  $\text{Cu}^{\text{II}}(\text{dien})(2\text{-Melm})$ ,  $\text{Cu}^{\text{II}}(2\text{-Melm})_2(\text{OAc})_2$ , and  $\text{Cu}^{\text{II}}\text{-}\alpha\beta(13\text{-}21)\text{K16A}$  complexes. This might arise from weak spin–spin interaction of  $\text{Cu}^{\text{II}}$  in the fibrils. A comprehensive EPR simulation analysis of the  $\text{Cu}^{\text{II}}$  model and  $\alpha\beta(13\text{-}21)$  spectra will be presented in a future publication.

### ESEEM spectroscopy of mono- and bis-imidazole $\text{Cu}^{\text{II}}$ model complexes

Figure 2 shows the powder three-pulse ESEEM waveform and corresponding FT for the mono-imidazole complex  $\text{Cu}^{\text{II}}(\text{dien})(2\text{-Melm})$ . The ESEEM was collected at the maximum ESE amplitude in the EPR spectrum and at a  $\tau$  value of 310 ns. ESEEM at

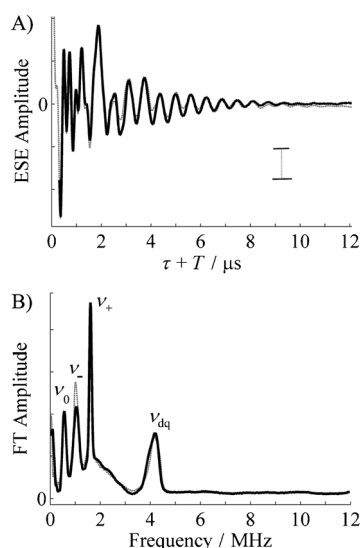


**Figure 2.** Experimentally measured powder three-pulse ESEEM and Fourier transform for  $[\text{Cu}^{\text{II}}(\text{dien})(2\text{-Melm})]$ , together with the overlaid simulation (dashed curves). In the ESEEM panel, the vertical scale bar corresponds to 25% of the constant echo amplitude at  $\tau + T = 12 \mu\text{s}$ . Experimental conditions: sample temperature 6 K, microwave frequency 8.772 GHz, magnetic field strength 3030 G, initial  $\tau$  value  $-190 \text{ ns}$ ,  $\tau$  increment  $20 \text{ ns}$ ,  $\pi/2$  pulse width  $20 \text{ ns}$ , pulse repetition rate  $120 \text{ Hz}$ , 64 pulses per repetition, average of two accumulations.

different  $\tau$  and microwave frequency/magnetic field values has previously been reported for the  $\text{Cu}^{\text{II}}(\text{dien})(2\text{-Melm})$  complex.<sup>[48]</sup> The ESEEM in Figure 2 exhibits a pattern of deep and sustained modulation in the time domain, together with corresponding narrow lines in the frequency domain; these are characteristic of coupling to  $^{14}\text{N}$  under the condition of exact cancellation: specifically, to the remote nitrogen of imidazole.<sup>[44,49]</sup> The exact cancellation condition holds when the  $^{14}\text{N}$  super-hyperfine (shf) and  $^{14}\text{N}$  nuclear Zeeman contributions approximately cancel for one electron spin manifold ( $A/2 \approx \nu_{\text{N}}$ , where  $A$  is the shf coupling constant and  $\nu_{\text{N}}$  is the free nuclear frequency), which creates a near zero-field condition in one electron spin manifold (the  $m_s = +1/2$ , or  $\alpha$ -, manifold, for isotropic shf coupling constant values,  $A_{\text{iso}} > 0$ ). The energy level separations in this manifold are dominated by the nuclear quadrupole inter-

action (nqi). The ESEEM Fourier transform (FT) for  $\text{Cu}^{\text{II}}(\text{dien})(2\text{-Melm})$  in Figure 2B shows three narrow lines positioned at 0.55, 1.04, and 1.61 MHz, which correspond to the  $\nu_0$ ,  $\nu_-$ , and  $\nu_+$  nqi frequencies (expected relationship  $\nu_0 + \nu_- = \nu_+$ ). The broad feature, centered at 4.2 MHz, corresponds to the  $\Delta m_i = \pm 2$ , or “double quantum” ( $\nu_{\text{dq}}$ ), splitting in the electron spin manifold in which the  $^{14}\text{N}$  shf and nuclear Zeeman contributions are additive (here the  $m_s = -1/2$ ,  $\beta$ -manifold). This feature is broadened by the dipolar shf coupling. The features corresponding to the  $\Delta m_i = \pm 1$  splittings, which overlap the  $\nu_0$ ,  $\nu_-$ , and  $\nu_+$  features, are broadened by the dipolar anisotropy, and are generally not resolved in exact cancellation ESEEM. There are no features at frequencies higher than  $\nu_{\text{dq}}$ , as anticipated for a mono-imidazole complex.

Figure 3 shows the powder three-pulse ESEEM waveform and corresponding FT for the bis-*cis*-imidazole complex  $\text{Cu}^{\text{II}}(2\text{-Melm})_2(\text{OAc})_2$ , of known structure.<sup>[50]</sup> The waveform and FT also

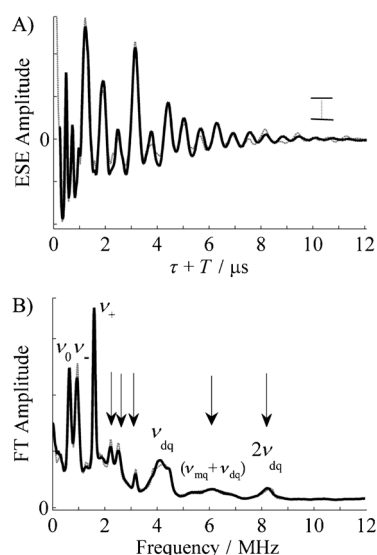


**Figure 3.** Experimentally measured powder three-pulse ESEEM and Fourier transform for  $[\text{Cu}^{\text{II}}(2\text{-Melm})_2(\text{OAc})_2]$ , together with the overlaid simulation (dashed curve). In the ESEEM panel, the vertical scale bar corresponds to 25% of the constant echo amplitude at  $\tau + T = 12 \mu\text{s}$ . In the Fourier transform panel, arrows indicate combination lines that correspond to the labeled fundamental lines. Simulation parameters are listed in Table 1. Experimental conditions: sample temperature 6 K, microwave frequency 8.772 GHz, magnetic field strength 3030 G,  $\tau$  value  $310 \text{ ns}$ , initial  $\tau + T$  value  $-190 \text{ ns}$ ,  $\tau$  increment  $20 \text{ ns}$ ,  $\pi/2$  pulse width  $20 \text{ ns}$ , pulse repetition rate  $120 \text{ Hz}$ , 64 pulses per repetition, one accumulation.

show the characteristic exact cancellation pattern of coupling to the remote  $^{14}\text{N}$  of the imidazole ring.<sup>[44,49]</sup> The FT in Figure 3 shows the fundamental nqi  $\nu_0$ ,  $\nu_-$ , and  $\nu_+$  lines at 0.61, 0.91, and 1.57 MHz, respectively, and the  $\nu_{\text{dq}}$  feature at 4.08 MHz. The three nqi and the  $\nu_{\text{dq}}$  lines appear at frequencies slightly shifted ( $< 10\%$ ) relative to those for the  $\text{Cu}^{\text{II}}(\text{dien})(2\text{-Melm})$  complex; this indicates a subtle difference in the electronic structure around the remote  $^{14}\text{N}$  nuclei in the two complexes, as would be expected from the difference in position of the alkyl substitution on the imidazole ring. The single set of narrow nqi fundamental features (line widths comparable to

the corresponding features in Figure 2) indicates that the two remote  $^{14}\text{N}$  nuclei in the complex have the same shf and nqj couplings, to within the resolution of the ESEEM experiment. In addition to the set of “fundamental” features observed for the mono-imidazole model, the  $\text{Cu}^{\text{II}}$ -bis-imidazole ESEEM shows “combination” lines that are positioned at sums of the fundamental frequencies. The combination lines are marked by arrows in Figure 3. These combination features arise from relatively low-probability, simultaneous nuclear spin-flip transitions between the two remote imidazole  $^{14}\text{N}$  nuclear spin states. Prominent features are observed at 2.20 ( $\nu_0 + \nu_+$ ), 2.49 ( $\nu_- + \nu_+$ ), and 3.16 ( $2\nu_+$ ) MHz. The weak feature from approximately 7.0 to 8.5 MHz represents the double quantum combination feature ( $2\nu_{\text{dq}}$ ), which corresponds to the combination of the  $\Delta m_i = \pm 2$  splittings in the noncancellation electron spin manifold of each coupled remote  $^{14}\text{N}$  nucleus. The feature, which is intermediate between the  $\nu_{\text{dq}}$  and  $2\nu_{\text{dq}}$  features, arises from combination of the  $\Delta m_i = \pm 2$  and  $\Delta m_i = \pm 1$  (denoted as monoquantum, “mq”) splittings in the noncancellation electron spin manifold, and is denoted  $\nu_{\text{mq}} + \nu_{\text{dq}}$  in Figure 3.

#### ESEEM spectroscopy of $\text{Cu}^{\text{II}}$ -A $\beta$ (13–21) mutant complexes

Figure 4 shows the powder three-pulse ESEEM waveform ( $\tau = 310$  ns) and the corresponding FT for the mono-imidazole complex<sup>[30]</sup>  $\text{Cu}^{\text{II}}$ -A $\beta$ (13–21)K16A. ESEEM at a different  $\tau$  value (156 ns) has been reported for this complex.<sup>[30]</sup> The ESEEM in Figure 4 is characteristic of coupling to the remote nitrogen of imidazole under the condition of exact cancellation.<sup>[44,49]</sup> As would be expected for the mono-imidazole equatorial coordi-

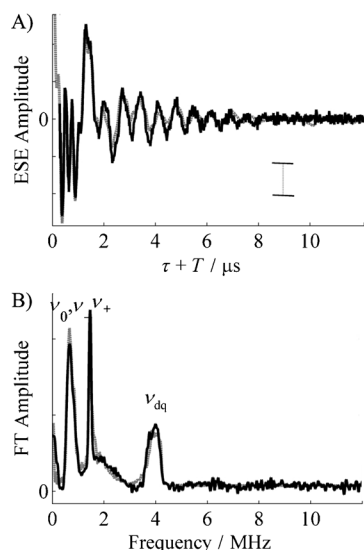


**Figure 4.** Experimentally measured powder three-pulse ESEEM and Fourier transform for  $[\text{Cu}^{\text{II}}\text{-A}\beta(13\text{--}21)\text{K16A}]$ , together with the overlaid simulation (dashed curve). In the ESEEM panel, the vertical scale bar corresponds to 25% of the constant echo amplitude at  $\tau + T = 12$   $\mu\text{s}$ . Experimental conditions: sample temperature 6 K, microwave frequency 8.831 GHz, magnetic field strength 3050 G, initial  $\tau$  value  $-190$  ns,  $\tau$  increment 20 ns,  $\pi/2$  pulse width 20 ns, pulse repetition rate 120 Hz, 64 pulses per repetition, average of two accumulations.

nation in  $\text{Cu}^{\text{II}}$ -A $\beta$ (13–21)K16A,<sup>[30]</sup> only the fundamental ESEEM features are observed.

Figure 5 shows the powder three-pulse ESEEM waveform and corresponding FT for the bis-imidazole complex  $\text{Cu}^{\text{II}}$ -A $\beta$ (13–21)H14A. ESEEM at a different  $\tau$  value (156 ns) has been

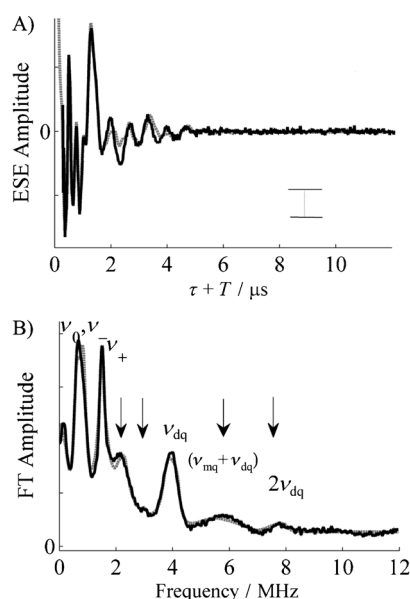


**Figure 5.** Experimentally measured powder three-pulse ESEEM and Fourier transform for  $\text{Cu}^{\text{II}}$ -Ac-A $\beta$ (13–21)H14A, together with the overlaid simulation (dashed curve). In the ESEEM panel, the vertical scale bar corresponds to 25% of the constant echo amplitude at  $\tau + T = 12$   $\mu\text{s}$ . In the Fourier transform panel, arrows indicate combination lines that correspond to the labeled fundamental lines. Simulation parameters are listed in Table 1. Experimental conditions: sample temperature 6 K, microwave frequency 8.831 GHz, magnetic field strength 3050 Gauss,  $\tau$  value 310 ns, initial  $\tau + T$  value  $-190$  ns,  $\tau$  increment 20 ns,  $\pi/2$  pulse width 20 ns, pulse repetition rate 120 Hz, 64 pulses per repetition, 48 accumulation.

reported for this complex.<sup>[30]</sup> In addition to the fundamental features, which show unresolved  $\nu_0$  and  $\nu_-$  lines, weak combination lines are observed; these correspond to the ( $\nu_0/\nu_- + \nu_+$ ) and ( $2\nu_+$ ) frequencies, as would be expected for the previously assigned<sup>[30]</sup> equatorial bis-histidine imidazole coordination. As shown in Figure 5,  $\text{Cu}^{\text{II}}$ -A $\beta$ (13–21)H14A ESEEM, collected at  $\tau = 310$  ns, also shows the  $\nu_{\text{mq}} + \nu_{\text{dq}}$  and  $2\nu_{\text{dq}}$  features. The relatively narrow, single-peak line shape of the  $2\nu_{\text{dq}}$  feature, which has a maximum at approximately 7.8 MHz, is similar to the  $2\nu_{\text{dq}}$  line shape for the  $\text{Cu}^{\text{II}}(2\text{-Melm})_2(\text{OAc})_2$  equatorial bis-*cis*-imidazole complex, and distinct from the broader, twin-peak  $2\nu_{\text{dq}}$  line shape of the  $\text{Cu}^{\text{II}}(\text{him})_2(\text{NO}_3)_2$  equatorial bis-*trans*-imidazole complex.<sup>[43]</sup>

#### Simulation of the $^{14}\text{N}$ ESEEM from the different $\text{Cu}^{\text{II}}$ complexes

Simulations of the ESEEM in Figures 2–5 are shown as overlaid dashed curves. The best-fit simulation parameters, and the simultaneous confidence regions at the 99% confidence level, are listed in Table 1. The principal values of the shf tensor, the nuclear quadrupole coupling constant ( $e^2qQ/h$ ), and the elec-

**Table 1.** ESEEM simulation parameters for the Cu<sup>II</sup>-imidazole model and A $\beta$ (13–21) complexes. The best-fit values and the simultaneous confidence region at the 99% confidence level are shown for each adjustable parameter. For each complex, the best-fit values for each simulation parameter are shown in the left-hand column, and the upper and lower limits of the simultaneous confidence regions for the parameters are given in the right-hand column.

Sample	Cu <sup>II</sup> (dien)(2-Melm)		Cu <sup>II</sup> (2-Melm) <sub>2</sub> (OAc) <sub>2</sub>		Cu <sup>II</sup> -A $\beta$ (13–21)K16A		Cu <sup>II</sup> -Ac-A $\beta$ (13–21)H14A	
A <sub>x</sub> [MHz]	2.41	2.44	2.43	2.44	2.12	2.17	2.25	2.29
A <sub>y</sub> [MHz]	1.94	2.38		2.41		2.08		2.20
A <sub>z</sub> [MHz]	1.42	1.98	1.77	1.85	1.80	1.88	1.82	1.86
e <sup>2</sup> qQ/h [MHz]	1.71	1.88		1.70		1.73		1.77
$\eta$	0.64	1.47	1.40	1.42	0.90	0.95	1.25	1.33
$\alpha_Q$ [°]	64	1.38		1.38		0.86		1.16
$\beta_Q$ [°]	22	1.72	1.64	1.64	1.51	1.52	1.52	1.53
$\gamma_Q$ [°]	20	1.70		1.63		1.50		1.51
$\alpha_A$ [°]	–	0.63	0.72	0.71	0.71	0.74	0.82	0.83
$\beta_A$ [°]	–			0.71		0.70		0.81
$\gamma_A$ [°]	–	64	75	20	24	228	246	360
		54	54	15	15	217	360	357
		27	18	24	9	10	67	355
		16		15		7		70
		32	359	3	291	306	291	65
		9		353		285		297
			25	30	–	–	1.0	288
				14				6
			132	143	–	–	113	351
				112				122
			312	320	–	–	299	105
				302				305
								292

is rotated through the Euler angles, [ $\alpha_A$   $\beta_A$   $\gamma_A$ ], displays the simultaneous confidence intervals at the 99% confidence level.

In order to assess the match of the physical model and X-ray crystallographic structure, we superposed the shf PAS onto the atomic coordinates of the X-ray structure,<sup>[50]</sup> by using the shf PAS/molecular PAS relationship derived from the single-crystal ESEEM studies.<sup>[51,52]</sup> The calculated physical model, which is based on the X-ray crystallographic coordinates, is shown in Figure 7A, and the structure of the complex, as determined by X-ray crystallography,<sup>[50]</sup> is shown in Figure 7B. The calculated model displays reasonable agreement with the ESEEM-derived physical model in Figure 6. In particular, the x-

tric field gradient (efg) asymmetry parameter ( $\eta$ ) for Cu<sup>II</sup>(dien)-(2-Melm) are comparable to values reported previously.<sup>[48]</sup> The  $A_{iso}$  values for Cu<sup>II</sup>(dien)(2-Melm), Cu<sup>II</sup>(2-Melm)<sub>2</sub>(OAc)<sub>2</sub>, and Cu<sup>II</sup>-A $\beta$ (13–21)H14A lie in the 1.7–1.9 MHz range, and the principal values of the dipolar shf tensors for the complexes all approximate the  $[A \ 0.2A \ -A]$  form common to 2- and 4-alkyl-substituted imidazole ligands to Cu<sup>II</sup>.<sup>[51–53]</sup> The electronic structure of the imidazole ring and the coupling of the unpaired spin density with the remote <sup>14</sup>N nuclei are therefore relatively constant across the four complexes. The narrow confidence regions for the shf and nqi parameters in Table 1 show a high relative certainty for the best-fit values and indicate that the parameters are strong determinants of the experimentally observed ESEEM (a wide confidence region indicates that the parameter is poorly constrained). The excellent quality of the simulations and the narrow confidence regions for the Cu<sup>II</sup>-bis-imidazole complexes provide further support for the assumption of comparable shf and nqi parameters for the two remote <sup>14</sup>N atoms in each complex.

## Discussion

### Mutual orientation of imidazole ligands in the Cu<sup>II</sup>(2-Melm)<sub>2</sub>(OAc)<sub>2</sub> complex

Figure 6 shows the physical model of the imidazole remote <sup>14</sup>N shf principal axis system (PAS) orientations in the Cu<sup>II</sup>(2-Melm)<sub>2</sub>(OAc)<sub>2</sub> complex, constructed by use of the Euler angles in Table 1. A stereoplot of the physical model is shown in Figure S1 in the Supporting Information. The shf PAS (black), that

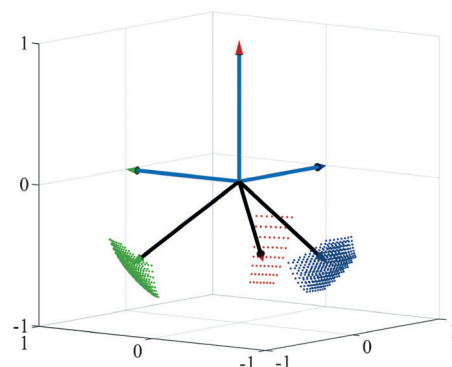


**Figure 6.** Physical model of the mutual orientation of the two remote <sup>14</sup>N shf PAS in [Cu<sup>II</sup>(2-Melm)<sub>2</sub>(OAc)<sub>2</sub>], derived from the powder <sup>14</sup>N ESEEM. The hatched surface represents the simultaneous confidence interval at the 99% level of confidence. Axis color code: x (blue), y (green), z (red).

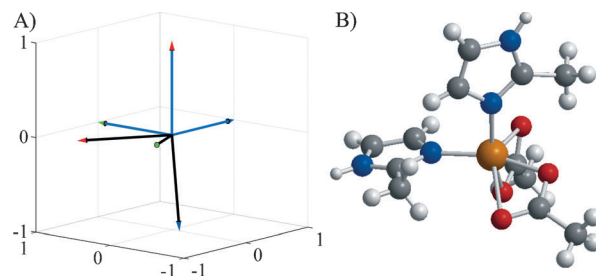


**Figure 7.** Calculated physical model and molecular structure of the Cu<sup>II</sup>(2-Melm)<sub>2</sub>(OAc)<sub>2</sub> complex. A) Calculated mutual orientation of the imidazole remote <sup>14</sup>N shf PAS in the Cu<sup>II</sup>(2-Melm)<sub>2</sub>(OAc)<sub>2</sub> complex, based on the X-ray crystallographic structure,<sup>[50]</sup> and the relation of the shf PAS to the imidazole molecular PAS.<sup>[51,52]</sup> Axis color code: x (blue), y (green), z (red). B) Molecular model based on the X-ray crystal structure.<sup>[50]</sup>



axes in each model are approximately perpendicular, which is characteristic of the *bis-cis* coordination mode. The deviations of the ESEEM-derived and calculated structures from agreement, beyond the confidence regions of the angular parameters, are attributed to differences between the crystal and glassy-solution structures of the complexes. Differences in the shf PAS orientations between the crystal and frozen glassy-solution structures would be expected for the  $\text{Cu}^{\text{II}}(2\text{-Melm})_2(\text{OAc})_2$  complex, because rotation of each imidazole ring about the  $\text{Cu}^{\text{II}}$ -ligand axis is possible. A difference in the imidazole rotamer states for the complexes in the crystal and in frozen glassy solution is supported by the fact that it is possible to rotate the two shf PAS in the physical model about the *x*-axes, which coincide with the proximal  $\text{N}-\text{Cu}^{\text{II}}$  bond direction, to achieve a very good match with the shf PAS determined for the X-ray crystallographic structure (Figure S2).

#### Assessment of the ESEEM method for determination of the bis-imidazole coordination geometry in $\text{Cu}^{\text{II}}$ complexes

We had previously reported a physical model for the *bis-trans*-imidazole complex<sup>[43]</sup>  $\text{Cu}^{\text{II}}(\text{him})_2(\text{NO}_3)_2$  and found excellent agreement of this model with the X-ray crystallographic structure.<sup>[46]</sup> The superposition of the shf PAS for  $\text{Cu}^{\text{II}}(\text{him})_2(\text{NO}_3)_2$  onto the atomic coordinates of the X-ray structure for  $\text{Cu}^{\text{II}}(\text{him})_2(\text{NO}_3)_2$ <sup>[46]</sup> (Figure S3) by use of the shf PAS/molecular PAS relationship derived from the single-crystal ESEEM studies<sup>[51,52]</sup> further quantifies the agreement with the reported physical model.<sup>[43]</sup> In the case of the *bis-trans*-imidazole complex, the deviations between the two models are within the angular range of the confidence intervals for the Euler angles, at the 99% confidence level. This is to be expected, because rotation of the imidazole rings about the  $\text{Cu}^{\text{II}}$ -ligand axis is constrained by the bidentate equatorial histamine coordination in the  $\text{Cu}^{\text{II}}(\text{him})_2$  complex.

The reasonable agreement, within the limits expected for crystal versus glassy frozen solvent conditions, of the powder ESEEM-derived physical models for the mutual orientation of the imidazole remote  $^{14}\text{N}$  PAS with that calculated from the combined single-crystal ESEEM and X-ray crystallographic results demonstrates that the powder  $^{14}\text{N}$  ESEEM experiment and numerical simulation approach, based on analysis of the  $\nu_{\text{mq}} + \nu_{\text{dq}}$  and  $2\nu_{\text{dq}}$  line shapes, is capable of accurately specifying the mutual orientation, to within the confidence intervals of the angular parameters. In contrast, in the general case of a  $\text{Cu}^{\text{II}}$ -bis-imidazole complex of unknown structure and unknown relation of the shf PAS to the imidazole molecular PAS, the *cis* or *trans* coordination mode cannot be uniquely determined. The finding of a rotation matrix with no eigenvalue of  $-1$  does, however, introduce the constraint that the mode is not *trans*. If, for example, the two shf PAS of the two imidazole moieties in a *bis-trans* configuration are related by a rotational matrix **R**, then there must exist a vector **v**, corresponding to the bonding direction of the proximal  $^{14}\text{N}$  and  $\text{Cu}^{\text{II}}$ , such that, when rotated by **R**, becomes  $-\mathbf{v}$ . The relationship  $\mathbf{R}\mathbf{v} = -\mathbf{v}$  requires **R** to have an eigenvalue of  $-1$ , corresponding to a  $180^\circ$  rotation about some reference axis. An eigenvalue of  $-1$  is not

sufficient, however, for the assignment of the *bis-trans* configuration. Information about the direction of the proximal  $^{14}\text{N}-\text{Cu}^{\text{II}}$  bond relative to the shf PAS is required.

In the case of a known relation of the shf PAS to the imidazole molecular PAS, the coordination mode can be uniquely determined, in addition to the mutual orientation of the imidazole molecular PAS. Therefore, with the inclusion of the shf PAS/molecular PAS correlation from the single-crystal ESEEM studies,<sup>[51,52]</sup> the *bis-cis*- or *bis-trans*-imidazole coordination mode of the complex can be determined.

#### Mutual orientation of imidazole ligands in the $\text{Cu}^{\text{II}}$ -Ac- $\beta(13-21)$ H14A peptide

Figure 8 depicts the physical model of the relative orientation of the shf PAS for  $\text{Cu}^{\text{II}}$ -Ac- $\beta(13-21)$ H14A, based on the Euler angles listed in Table 1. The *x*-axes in the model are approxi-

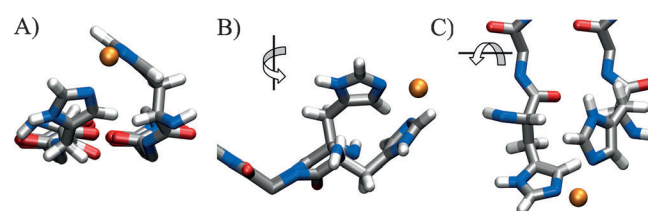


**Figure 8.** Molecular structural model for the local  $\text{Cu}^{\text{II}}$  coordination site in the context of the global Ac- $\beta(13-21)$ H14A fibril structural model. The local interaction of  $\text{Cu}^{\text{II}}$  with two  $\beta$ -strands from the  $\beta$ -sheet is shown. A) View along  $\beta$ -strand axis. Fibril axis is along horizontal. B) View along fibril axis. The view is rotated by  $90^\circ$ , relative to panel A, as shown. C) View of side of  $\beta$ -sheet. Fibril axis is along horizontal. The view is rotated by  $90^\circ$ , relative to panel A, as shown. Atom color code:  $\text{Cu}^{\text{II}}$  orange, oxygen red, nitrogen blue, carbon gray, hydrogen white.

mately perpendicular, as shown by the confidence region of  $75^\circ$  to  $110^\circ$ . Perpendicular *x*-axes are characteristic of the *bis-cis*-imidazole coordination mode, as demonstrated for the  $\text{Cu}^{\text{II}}(2\text{-Melm})_2(\text{OAc})_2$  complex. Therefore, we conclude that the  $\text{Cu}^{\text{II}}$  in fibrils of Ac- $\beta(13-21)$ H14A is coordinated in the equatorial plane by two histidine imidazole units in the *cis* geometry. Our ability to simulate the results by using a discrete model of  $\text{Cu}^{\text{II}}$ -remote  $^{14}\text{N}$  coupling (single set of shf, nqi, and orientation simulation parameters), indicates a single coordination geometry for  $\text{Cu}^{\text{II}}$  with the Ac- $\beta(13-21)$ H14A peptide in the fibril. This is consistent with the homogeneous fibril morphology on the meso scale, which is shown by electron microscopy studies.<sup>[30]</sup>

#### $\text{Cu}^{\text{II}}$ -bis-*cis*-His coordination in the context of the Ac- $\beta(13-21)$ H14A fibril

In the structural model for fibrils of Ac- $\beta(13-21)$ H14A, individual peptides, in a  $\beta$ -strand configuration, combine to form a parallel, in-register  $\beta$ -sheet structure that extends along the inter-strand, hydrogen-bonding direction, to define the long axis of the fibril.<sup>[30]</sup> Multiple  $\beta$ -sheets stack, or laminate, in a direction perpendicular to the long axis.<sup>[30]</sup> The inter- $\beta$ -strand,

backbone-to-backbone spacing within each sheet is 4.7 Å, and the inter-sheet separation is approximately 10 Å.<sup>[30,54]</sup>

Figure 8 depicts a structural model for the local Cu<sup>II</sup> coordination site in the context of the global Ac-Aβ(13–21)H14A fibril structural model.<sup>[30]</sup> The molecular modeling program Macro-model (version 9.9, Schrödinger, LLC, New York, NY) was used to construct the model, with incorporation of the following constraints: 1) intra-sheet, bis-*cis*-imidazole coordination by H13 on adjacent peptides, with hydrogen-bonded peptides separated by 4.7 Å,<sup>[30]</sup> 2) mutual orientation of the two imidazole rings from the physical model (Figure 9), 3) angle of 93°

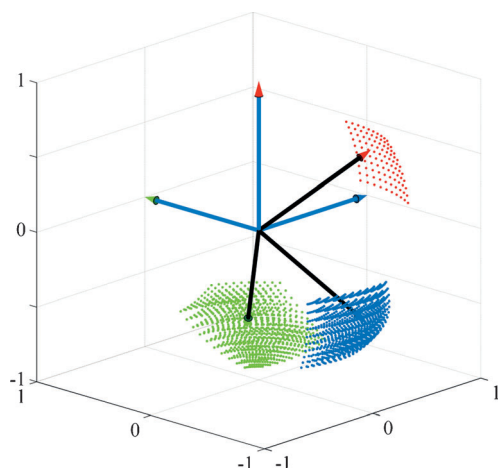


**Figure 9.** Physical model of the mutual orientation of the two remote <sup>14</sup>N shf PAS in [Cu<sup>II</sup>-Ac-Aβ(13–21)H14A], derived from the powder <sup>14</sup>N ESEEM. The hatched surface represents the simultaneous confidence interval at the 99% level of confidence. Axis color code: x (blue), y (green), z (red).

between the proximal <sup>14</sup>N–Cu<sup>II</sup> bonds, which corresponds to the center of the confidence region (Figure 9), 4) distance of 2.0 Å [characteristic of the <sup>14</sup>N–metal distance in Cu<sup>II</sup>-imidazole complexes, including the bis-*trans*- (2.03 Å) and bis-*cis*-imidazole (1.97, 1.98 Å) model Cu<sup>II</sup> complexes<sup>[46,50]</sup>] between the proximal (directly coordinated) imidazole <sup>14</sup>N and Cu<sup>II</sup>, 5) direct coordination by imidazole ring Nε atoms, 6) fixed coordinates for all peptide atoms, other than atoms of H13 and the acetyl capping group, and 7) adherence to local steric constraints, by use of the MMFF94<sup>[55]</sup> force field. As depicted in Figure 8, the bis-*cis* coordination mode is accommodated by the 4.7 Å intra-strand distance. The bis-*cis* mode is obligatory for Cu<sup>II</sup> binding, relative to the bis-*trans* mode, because *trans* coordination significantly distorts the N-terminal region and thus destabilizes the intra-β-strand interactions distal to the Cu<sup>II</sup> site.

The bis-*cis*-imidazole coordination mode partially resolves the structure of the intra-sheet coordination of Cu<sup>II</sup> at the N-terminal region of the fibrils and is consistent with the structural model proposed for Ac-Aβ(13–21)H14A fibrils.<sup>[30]</sup> Figure 10 shows a representation of the global Ac-Aβ(13–21)H14A fibril model that incorporates the local Cu<sup>II</sup> site geometry. The pairwise interaction of the peptides with Cu<sup>II</sup>, which creates an alternating [–metal-vacancy–]<sub>n</sub> pattern with an approximately

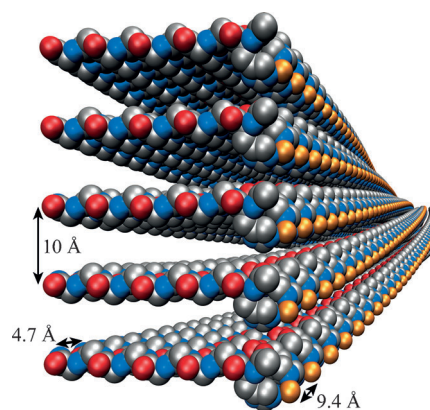


**Figure 10.** Representation of the molecular structure model for the Cu<sup>II</sup>-Ac-Aβ(13–21)H14A amyloid fiber. The Cu<sup>II</sup> and H13 positions correspond to the local site geometry, displayed in Figure 8A–C. Only peptide backbone and histidine side chains are shown, for clarity. Distances correspond to the hydrogen-bonded, intra-sheet peptide spacing (4.7 Å), intra-sheet spacing of Cu<sup>II</sup> sites (9.4 Å), and β-sheet lamination distance (10 Å). Atom color code: Cu<sup>II</sup> orange, oxygen red, nitrogen blue, carbon grey, hydrogen white.

9.4 Å periodicity along the N-terminal region of the β-sheet, is accommodated by the global β-sheet structure.

## Conclusions

We thus propose that Cu<sup>II</sup>-induced acceleration of Ac-Aβ(13–21)H14A fibril formation arises from the two following factors: 1) the β-sheet structure is stabilized by Cu<sup>II</sup> coordination, this reduces the monomer dissociation rate, and 2) Cu<sup>II</sup> coordination aligns and stabilizes β-strand peptide pair precursors that integrate into the fibril, with a minimum reorganization energy, thus increasing the effective peptide association rate.

## Experimental Section

**Synthesis of model complexes and peptides and EPR sample preparation:** All chemicals used in the syntheses were obtained from commercial sources (Sigma–Aldrich or Fisher) and used without further purification.

**Cu<sup>II</sup>(dien)(2-Melm):** The Cu<sup>II</sup>(dien)(2-Melm) complex was prepared as described by McCracken et al.<sup>[48]</sup> Briefly, copper(II) diethylenetriamine acetate (2.6 mg), copper(II) acetate (5.0 mg), and 2-methylimidazole (41.0 mg) were mixed in water (5 mL), and ethylene glycol was added to form a 1:1 ethylene glycol/water solution. The pH was adjusted to 8.0. The solution was frozen to a glass in a quartz EPR tube (4 mm outer diameter) and stored in liquid nitrogen (77 K).

**Cu<sup>II</sup>(him)<sub>2</sub>(NO<sub>3</sub>)<sub>2</sub>:** The [Cu<sup>II</sup>(him)<sub>2</sub>(NO<sub>3</sub>)<sub>2</sub>] complex was prepared by the procedure described by Zhang et al.<sup>[46]</sup> Briefly, histamine dihydrochloride (25.95 mg) and sodium hydroxide (1 M, 0.28 mL) in water (2.72 mL) were added to ethanol (3.93 mL) containing copper(II) nitrate trihydrate (1 M, 0.07 mL). The mixture was then added to ethylene glycol (7 mL), placed in a quartz EPR tube (4 mm outer diameter), frozen to a glass, and stored in liquid nitrogen.

**Cu<sup>II</sup>(2-Melm)<sub>2</sub>(OAc)<sub>2</sub>:** The [Cu<sup>II</sup>(2-Melm)<sub>2</sub>(OAc)<sub>2</sub>] complex was prepared as described by Abuhijleh et al.<sup>[50]</sup> Cu<sup>II</sup> acetate (0.5 g) and 2-methylimidazole (1.0 g) were dissolved in chloroform (10 mL) and methanol (2.5 mL). The mixture was stirred for 30 min at 50 °C. The mixture was filtered, and diethyl ether (15 mL) was added to the filtrate. The filtrate was stirred again for 10 min, followed by the addition of diethyl ether (5 mL). The solution was filtered under reduced pressure and washed with diethyl ether and chloroform. The solid was air dried and recrystallized from methanol/diethyl ether. The crystals were dissolved in methanol/chloroform 1:4 in a quartz EPR tube (4 mm outer diameter), and the solution was then frozen to a glass and stored in liquid nitrogen.

**Aβ(13–21) peptides:** The Aβ(13–21)H14A peptide was synthesized as described.<sup>[30]</sup> The peptide was dissolved in buffer (pH 7.2) containing HEPES (25 mM) and NaCl (10 mM). After incubation of the sample for two weeks, fibrils had been produced, as verified by electron microscopy.<sup>[30]</sup> Copper was added as CuCl<sub>2</sub>. The Ac-Aβ(13–21)H14/Cu<sup>II</sup> ratio was 2:1. The peptide Aβ(13–21)K16A was synthesized as described.<sup>[30]</sup> The peptide was dissolved in buffer (pH 5.6) containing 2-(4-morpholino)ethanesulfonic acid (MES, 25 mM) and NaCl (10 mM). The Aβ(13–21)K16A/Cu<sup>II</sup> ratio was 1:1. Samples for EPR and ESEEM were mixed with an equal volume of ethylene glycol, transferred to a quartz EPR tube (4 mm outer diameter), and then frozen to a glass and stored in liquid nitrogen.

**EPR spectroscopy:** X-band continuous-wave EPR spectroscopy was performed with a Bruker ELEXSYS E500 EPR spectrometer with an ER 4123SHQE X-band cavity resonator and a Bruker ER 4131VT liquid nitrogen flow temperature control system. EPR spectra of the Cu<sup>II</sup> model and the Cu<sup>II</sup>-Aβ complexes were acquired at temperatures of 120 and 140 K, respectively.

#### ESEEM spectroscopy

**<sup>14</sup>N ESEEM of Cu<sup>II</sup>-imidazole complexes:** ESEEM sensitively detects the coupling of the unpaired electron spin ( $S = 1/2$ ) on Cu<sup>II</sup> with the “remote” (not directly coordinated) nitrogen nuclei (<sup>14</sup>N; nuclear spin,  $I = 1$ ) of equatorial imidazole ligands.<sup>[44]</sup> The electron-nuclear coupling condition that is characteristic of the Cu<sup>II</sup>-remote <sup>14</sup>N interaction, known as “exact cancellation”,<sup>[44, 49]</sup> leads to the presence in the ESEEM of modulation components that correspond to the remote <sup>14</sup>N shf and <sup>14</sup>N nqi energy level splittings. The shf principal tensor components—[ $A_x$ ,  $A_y$ ,  $A_z$ —and nqi parameters (nuclear quadrupole coupling constant and electric field gradient asymmetry parameter) and the relative orientation of the shf and nqi principal axis systems (PAS) are obtained from numerical simulations of the <sup>14</sup>N ESEEM. <sup>14</sup>N ESEEM has previously been used to determine the shf and nqi parameters for the imidazole remote <sup>14</sup>N in Cu<sup>II</sup> sites in copper proteins<sup>[48, 56]</sup> and in Cu<sup>II</sup> model complexes in frozen solution,<sup>[48, 56, 57]</sup> in single crystals,<sup>[51–53, 58, 59]</sup> and in a single crystal/powder comparison study.<sup>[60]</sup>

**Experimental:** ESEEM data were collected at 6 K with a home-built pulsed-EPR spectrometer by using the three-pulse ( $\pi/2$ - $\tau$ - $\pi/2$ - $T$ - $\pi/2$ - $\tau$ -echo) microwave pulse sequence with pulse-swapping.<sup>[61]</sup> The pulse-swapping sequence reduces the effective dead time to the intrinsic spectrometer dead time, which is the time required for the ring-down of the microwave pulse energy in the resonator to the level of the ESE signals, at the particular spins/Gauss values for the Cu<sup>II</sup> samples used in these studies (160–200 ns). The  $\tau$  value was selected from a scan of the  $\tau$  values, corresponding to the relationship  $\tau = \frac{n}{\nu_{\text{H}}}$ , where  $n = 1, 2, 3, \dots$  and  $\nu_{\text{H}}$  is the free precession frequency of the <sup>1</sup>H nucleus at the prevailing external magnetic field (3030 G). These  $\tau$  values correspond to  $\tau$  suppression<sup>[62]</sup> of the free <sup>1</sup>H contribution to the ESEEM. The  $2\nu_{\text{dq}}$  feature achieved

the largest amplitude at  $\tau$  values of 310 ns and 620 ns, but was near to, or within, the noise amplitude at the other  $\tau$  values. The  $\tau$  value of 310 ns was selected for analysis, because the shorter time period of the phase memory decay in the pulse-swapping sequence afforded the best signal-to-noise ratio, relative to  $\tau = 622$  ns. ESEEM was cosine Fourier transformed to generate ESEEM frequency spectra. The dead time modulation was reconstructed by use of the simulated ESEEM. All data processing was performed by using laboratory-written MATLAB (Mathworks, Natick, MA) code running on personal computers.

**ESEEM simulations:** Numerical simulations of the ESEEM were performed by using the OPTESIM ESEEM simulation and analysis software suite.<sup>[43]</sup> The stationary-state spin Hamiltonian for treatment of the interaction of the electron spin on Cu<sup>II</sup> with the remote <sup>14</sup>N nuclear spin is formulated with a shf coupling term, a nuclear Zeeman term, and a nqi term, as follows:<sup>[63]</sup>

$$H = h \vec{S} \mathbf{A} \vec{I} - g_N \beta_N \vec{B}_0 \cdot \vec{I} - \vec{I} \cdot \vec{I}' \cdot \mathbf{Q} \cdot \vec{I}' \quad (1)$$

where  $\beta_N$ ,  $\vec{S}$ , and  $\vec{I}$  are the nuclear magneton, electron spin operator, and nuclear spin operator, respectively,  $g_N$  is the nuclear  $g$  value,  $\mathbf{A}$  is the shf coupling tensor, and  $\mathbf{Q}$  is the nqi tensor.<sup>[64]</sup>  $I$  and  $I'$  indicate that the eigenfunctions of  $\mathbf{A}$  and  $\mathbf{Q}$  are, in general, different. The shf tensor has the principal components  $\mathbf{A} = [A_{xx}, A_{yy}, A_{zz}]$  and is composed of an isotropic part ( $A_{\text{iso}} = 1/3 \sum A_{ii}$ ) and a dipolar part ( $\mathbf{A} - A_{\text{iso}}$ ). The nqi tensor ( $\mathbf{Q}$ ) is defined by the nuclear quadrupole coupling constant ( $e^2 q Q / h$ ) and the electric field gradient (efg) asymmetry parameter ( $\eta$ ).<sup>[65]</sup> In its PAS, the traceless nqi tensor  $\mathbf{Q} = [Q_{xx}, Q_{yy}, Q_{zz}]$  is related to  $e^2 q Q / h$  and  $\eta$  by the following expressions:

$$Q_{zz} = \frac{e^2 q Q}{2I(2I-1)\hbar} \quad (2)$$

$$\eta = \frac{Q_{xx} - Q_{yy}}{Q_{zz}} \quad (3)$$

where  $|Q_{xx}| \geq |Q_{yy}| \geq |Q_{zz}|$ . In OPTESIM, the orientation between the nqi tensor PAS and the shf tensor PAS is defined by the Euler angles [ $\alpha_Q$ ,  $\beta_Q$ ,  $\gamma_Q$ ]. In systems with more than one coupled nucleus ( $N > 1$ ), the orientation of the shf PAS of each nucleus, relative to an arbitrary reference frame, is defined by the Euler angles [ $\alpha_A$ ,  $\beta_A$ ,  $\gamma_A$ ]. For the two remote <sup>14</sup>N couplings in the Cu<sup>II</sup>-bis-imidazole complexes studied here, [ $\alpha_A$ ,  $\beta_A$ ,  $\gamma_A$ ] are chosen to define the mutual orientation of the two shf PAS.

A coupled electron-single <sup>14</sup>N system is therefore parameterized by using the following eight adjustable parameters:  $A_{xx}$ ,  $A_{yy}$ ,  $A_{zz}$ ,  $\alpha_Q$ ,  $\beta_Q$ ,  $\gamma_Q$ ,  $e^2 q Q / h$ , and  $\eta$ . In the Cu<sup>II</sup>-bis-imidazole complexes, these eight parameters are assumed to be common to the two imidazole <sup>14</sup>N nuclei. The bis-imidazole complexes have  $\alpha_A$ ,  $\beta_A$ , and  $\gamma_A$  as additional adjustable parameters. The method for calculation of the simultaneous confidence region for each adjustable parameters, at a specific confidence level (here 99%), has been described.<sup>[43]</sup>

The ESEEM calculation in OPTESIM incorporates the full-density matrix diagonalization from the Mims treatment of ESEEM<sup>[63, 66]</sup> for evaluation of the transition frequencies and intensities, but uses a computationally efficient numerical procedure<sup>[18, 67, 68]</sup> for constructing the three-pulse modulation. In the case of a powder distribution, which is approximated well by the nominally octahedral Cu<sup>II</sup>-bis-imidazole complexes near the  $g_{\perp}$  position of the EPR spec-



trum,<sup>[45]</sup> a spherical average is calculated for the ESEEM. For more than one coupled nucleus ( $N > 1$ ), the computed spherical average in OPTESIM is performed by using a physical model that includes information about the particular arrangement of coupled nuclei relative to the paramagnet. This geometry is defined by the set of Euler angles,  $[\alpha_A \beta_A \gamma_A]$ , for each nucleus, which together specify the mutual orientation of the different shf PAS. The ESEEM is therefore calculated and combined at each powder orientation. A physical model has previously been used to simulate  $^{14}\text{N}$  ESEEM in a metal complex.<sup>[69]</sup> The three-pulse envelope modulation for the  $N=2$  electron-nuclear couplings is combined separately for the  $\alpha$ - and  $\beta$ -electron spin manifolds by using the following product rule:<sup>[70]</sup>

$$E_{\text{total}}(\tau, T) = \prod_i E_{\alpha,i}(\tau, T) + \prod_i E_{\beta,i}(\tau, T) \quad (4)$$

The automated optimization of the simulations used a genetic algorithm, followed by the Nelder–Mead simplex method. The optimization was performed on the experimental ESEEM wave forms only. The genetic algorithm had a starting population of 300. The genetic algorithm converged after approximately 100 generations, and the best individual was selected as the starting point for the simplex method. Simulations were run in parallel on a collection of personal computers, which were tasked with subsets of the powder orientation sampling vectors, under the Java-RMI-based distributed computational framework that is included in OPTESIM.<sup>[43]</sup>

**Relation between shf tensor PAS and molecular PAS of imidazole:** Single-crystal ESEEM studies of the  $\text{Cu}^{\text{II}}$ -mono-imidazole complex in  $\text{Cu}^{\text{II}}$ -doped crystals of L-histidine hydrochloride monohydrate<sup>[51]</sup> and in  $\text{Cu}^{\text{II}}$ -doped bis-(L-histinato)cadmium dihydrate,<sup>[52]</sup> determined, in addition to the shf and nqi parameters, the relation of the imidazole remote  $^{14}\text{N}$  shf and nqi tensors to the respective crystal axes.<sup>[51,52]</sup> This allowed the  $^{14}\text{N}$  shf PAS and nqi PAS to be related to the molecular frame of the imidazole. The  $A_z$  component is tilted by  $8^\circ$  relative to the imidazole ring plane normal. The  $A_x$  axis lies in the ring plane and makes an angle of  $13^\circ$  with the imidazole  $\text{N}_\delta\text{--N}_\epsilon$  axis. In these systems, the  $^{14}\text{N}$  dipolar shf tensor, which represents the through-space interaction between the unpaired electron distribution and the nucleus, has a rhombic form.<sup>[51]</sup> The orientation of the dipolar shf tensor in the molecular frame of the imidazole ring was accounted for by using a multi-point electron spin density model.<sup>[51,53]</sup> Density functional theory (DFT) calculations found a positive sign for the isotropic hyperfine coupling ( $A_{\text{iso}} > 0$ ) for the remote  $^{14}\text{N}$  nuclei in the two imidazole ligands in  $\text{Cu}^{\text{II}}$ -bis-histamine in frozen solution.<sup>[71]</sup> Collectively, the results show that the remote  $^{14}\text{N}$  dipolar shf tensor in different  $\text{Cu}^{\text{II}}$  complexes with 2- and 4-alkyl substituted imidazoles has the approximate rhombic form  $[A \ 0.2A\text{--}A]$ ,<sup>[51,52,56]</sup> to within 20% of the component values, which implies a comparable unpaired electron spin density distribution over the atoms of the imidazole rings and an associated common angular relation of the dipolar shf PAS to the imidazole molecular PAS.

## Acknowledgements

This work was supported, in part, by an Emory University Arts and Sciences Partnership Seed Funding Program grant. The authors acknowledge the Division of Chemical Sciences, Geosciences, and Biosciences, Office of Basic Energy Sciences of the U.S.

Department of Energy through Grant DE-ER15377 for peptide synthesis and analyses. Research reported in this publication was supported, in part, by the National Institute of Diabetes and Digestive and Kidney Diseases of the National Institutes of Health under Award Number R01 DK054514. The purchase of the Bruker E500 EPR spectrometer was funded by National Institutes of Health, National Center for Research Resources grant RR17767 and by Emory University.

**Keywords:** amyloid beta-peptides • bioinorganic chemistry • copper • EPR spectroscopy • ESEEM spectroscopy

- [1] Alzheimer's Association, *Alzheimer's Dementia* **2009**, 5, 234–270.
- [2] D. J. Selkoe, *Nat. Med.* **2011**, 17, 1060–1065.
- [3] D. J. Selkoe, *Science* **2002**, 298, 789–791.
- [4] P. W. Mantyh, J. R. Ghilardi, S. Rogers, E. Demaster, C. J. Allen, E. R. Stimson, J. E. Maggio, *J. Neurochem.* **1993**, 61, 1171–1174.
- [5] M. A. Lovell, J. D. Robertson, W. J. Teesdale, J. L. Campbell, W. R. Markesbery, *J. Neurol. Sci.* **1998**, 158, 47–52.
- [6] A. I. Bush, *Trends Neurosci.* **2003**, 26, 207–214.
- [7] L. M. Miller, Q. Wang, T. P. Telivala, R. J. Smith, A. Lanzirrotti, J. Miklossy, *J. Struct. Biol.* **2006**, 155, 30–37.
- [8] S. Parthasarathy, F. Long, Y. Miller, Y. Xiao, D. McElheny, K. Thurber, B. Ma, R. Nussinov, Y. Ishii, *J. Am. Chem. Soc.* **2011**, 133, 3390–3400.
- [9] A. I. Bush, W. H. Pettingell, G. Multhaup, M. D. Paradis, J. P. Vonsattel, J. F. Gusella, K. Beyreuther, C. L. Masters, R. E. Tanzi, *Science* **1994**, 265, 1464–1467.
- [10] D. Allsop, J. Mayes, S. Moore, A. Masad, B. J. Tabner, *Biochem. Soc. Trans.* **2008**, 36, 1293–1298.
- [11] D. R. Brown, F. Hafiz, L. L. Glasssmith, B. S. Wong, I. M. Jones, C. Clive, S. J. Haswell, *EMBO J.* **2000**, 19, 1180–1186.
- [12] M. Chattopadhyay, E. D. Walter, D. J. Newell, P. J. Jackson, E. Aronoff-Spencer, J. Peisach, G. J. Gerfen, B. Bennett, W. E. Antholine, G. L. Millhauser, *J. Am. Chem. Soc.* **2005**, 127, 12647–12656.
- [13] E. S. Riihimäki, J. M. Martinez, L. Kloo, *Phys. Chem. Chem. Phys.* **2008**, 10, 2488–2495.
- [14] R. M. Rasia, C. W. Bertoncini, D. Marsh, W. Hoyer, D. Cherny, M. Zweckstetter, C. Griesinger, T. M. Jovin, C. O. Fernandez, *Proc. Natl. Acad. Sci. USA* **2005**, 102, 4294–4299.
- [15] A. Binolfi, G. R. Lamberto, R. Duran, L. Quintanar, C. W. Bertoncini, J. M. Souza, C. Cervenansky, M. Zweckstetter, C. Griesinger, C. O. Fernandez, *J. Am. Chem. Soc.* **2008**, 130, 11801–11812.
- [16] L. Kevan, M. K. Bowman, *Modern Pulsed and Continuous-Wave Electron Spin Resonance*, Wiley, New York, **1990**.
- [17] A. Schweiger, *Angew. Chem.* **1991**, 103, 223–250; *Angew. Chem. Int. Ed. Engl.* **1991**, 30, 265–292.
- [18] S. A. Dikanov, Y. D. Tsvetkov, *Electron Spin Echo Envelope Modulation (ESEEM) Spectroscopy*, CRC Press, Boca Raton, **1992**.
- [19] P. Höfer, A. Grupp, G. Nebenführ, M. Mehring, *Chem. Phys. Lett.* **1986**, 132, 279–283.
- [20] B. K. Shin, S. Saxena, *Biochemistry* **2008**, 47, 9117–9123.
- [21] S. C. Drew, C. J. Noble, C. L. Masters, G. R. Hanson, K. J. Barnham, *J. Am. Chem. Soc.* **2009**, 131, 1195–1207.
- [22] P. Dorlet, S. Gambarelli, P. Faller, C. Hureau, *Angew. Chem.* **2009**, 121, 9437–9440; *Angew. Chem. Int. Ed.* **2009**, 48, 9273–9276.
- [23] B. Alies, H. Eury, C. Bijani, L. Rechignat, P. Faller, C. Hureau, *Inorg. Chem.* **2011**, 50, 11192–11201.
- [24] S. C. Drew, K. J. Barnham, *Acc. Chem. Res.* **2011**, 44, 1146–1155.
- [25] B.-k. Shin, S. Saxena, *J. Phys. Chem. A* **2011**, 115, 9590–9602.
- [26] C. D. Syme, R. C. Nadal, S. E. J. Rigby, J. H. Viles, *J. Biol. Chem.* **2004**, 279, 18169–18177.
- [27] J. W. Karr, H. Akintoye, L. J. Kaupp, V. A. Szalai, *Biochemistry* **2005**, 44, 5478–5487.
- [28] C. J. Sarell, C. D. Syme, S. E. J. Rigby, J. H. Viles, *Biochemistry* **2009**, 48, 4388–4402.
- [29] W. A. Gunderson, J. Hernandez-Guzman, J. W. Karr, L. Sun, V. A. Szalai, K. Warnecke, *J. Am. Chem. Soc.* **2012**, 134, 18330–18337.

- [30] J. Dong, J. M. Canfield, A. K. Mehta, J. E. Shokes, B. Tian, W. S. Childers, J. A. Simmons, Z. Mao, R. A. Scott, K. Warncke, D. G. Lynn, *Proc. Natl. Acad. Sci. USA* **2007**, *104*, 13313–13318.
- [31] K. Lu, J. Jacob, P. Thiyagarajan, V. P. Conticello, D. G. Lynn, *J. Am. Chem. Soc.* **2003**, *125*, 6391–6393.
- [32] Y. Liang, P. Guo, S. V. Pingali, S. Pabir, P. Thiyagarajan, K. M. Berland, D. G. Lynn, *Chem. Commun.* **2008**, 6522–6524.
- [33] T. P. J. Knowles, M. J. Buehler, *Nat. Nanotechnol.* **2011**, *6*, 469–479.
- [34] T. Scheibel, R. Parthasarathy, G. Sawicki, X.-M. Lin, H. Jaeger, S. L. Lindquist, *Proc. Natl. Acad. Sci. USA* **2003**, *100*, 4527–4532.
- [35] O. Carny, D. E. Shalev, E. Gazit, *Nano Lett.* **2006**, *6*, 1594–1597.
- [36] C. Hilbich, B. Kisterswoike, J. Reed, C. L. Masters, K. Beyreuther, *J. Mol. Biol.* **1992**, *228*, 460–473.
- [37] D. J. Gordon, J. J. Balbach, R. Tycko, S. C. Meredith, *Biophys. J.* **2004**, *86*, 428–434.
- [38] J. J. Dong, J. E. Shokes, R. A. Scott, D. G. Lynn, *J. Am. Chem. Soc.* **2006**, *128*, 3540–3542.
- [39] A. T. Petkova, W.-M. Yau, R. Tycko, *Biochemistry* **2006**, *45*, 498–512.
- [40] A. K. Paravastu, R. D. Leapman, W.-M. Yau, R. Tycko, *Proc. Natl. Acad. Sci. USA* **2008**, *105*, 18349–18354.
- [41] I. Bertini, L. Gonnelli, C. Luchinat, J. Mao, A. Nesi, *J. Am. Chem. Soc.* **2011**, *133*, 16013–16022.
- [42] M. Ahmed, J. Davis, D. Aucoin, T. Sato, S. Ahuja, S. Aimoto, J. I. Elliott, W. E. Van Nostrand, S. O. Smith, *Nat. Struct. Mol. Biol.* **2010**, *17*, 561–567.
- [43] L. Sun, J. Hernandez-Guzman, K. Warncke, *J. Magn. Reson.* **2009**, *200*, 21–28.
- [44] W. B. Mims, J. Peisach, *J. Chem. Phys.* **1978**, *69*, 4921–4930.
- [45] W. Weltner, *Magnetic Atoms and Molecules*, Scientific and Academic Editions, New York, **1983**.
- [46] C. G. Zhang, C. Y. Duan, Q. Hu, D. Y. Yan, *J. Chem. Crystallogr.* **1999**, *29*, 1153–1155.
- [47] M. Pasenkiewicz-Gierula, W. K. Subczynski, W. E. Antholine, *J. Phys. Chem. B* **1997**, *101*, 5596–5606.
- [48] J. McCracken, S. Pember, S. J. Benkovic, J. J. Villafranca, R. J. Miller, J. Peisach, *J. Am. Chem. Soc.* **1988**, *110*, 1069–1074.
- [49] H. L. Flanagan, D. J. Singel, *J. Chem. Phys.* **1987**, *87*, 5606–5616.
- [50] A. L. Abuhijleh, C. Woods, I. Y. Ahmed, *Inorg. Chim. Acta* **1991**, *190*, 11–17.
- [51] M. J. Colaneri, J. Peisach, *J. Am. Chem. Soc.* **1992**, *114*, 5335–5341.
- [52] M. J. Colaneri, J. Peisach, *J. Am. Chem. Soc.* **1995**, *117*, 6308–6315.
- [53] M. J. Colaneri, J. A. Potenza, H. J. Schugar, J. Peisach, *J. Am. Chem. Soc.* **1990**, *112*, 9451–9458.
- [54] T. S. Burkoth, T. L. S. Benzinger, V. Urban, D. M. Morgan, D. M. Gregory, P. Thiyagarajan, R. E. Botto, S. C. Meredith, D. G. Lynn, *J. Am. Chem. Soc.* **2000**, *122*, 7883–7889.
- [55] T. A. Halgren, *J. Comput. Chem.* **1999**, *20*, 720–729.
- [56] F. Jiang, J. McCracken, J. Peisach, *J. Am. Chem. Soc.* **1990**, *112*, 9035–9044.
- [57] W. M. Ames, S. C. Larsen, *Phys. Chem. Chem. Phys.* **2009**, *11*, 8266–8274.
- [58] M. J. Colaneri, J. Peisach, *J. Magn. Reson. Ser. A* **1993**, *102*, 360–363.
- [59] M. J. Colaneri, J. Vitali, J. Peisach, *Biochemistry* **2000**, *39*, 584–591.
- [60] J. J. Shane, P. A. A. W. Vanderheijden, E. J. Reijerse, E. Deboer, *Appl. Magn. Reson.* **1994**, *6*, 427–454.
- [61] J.-M. Fauth, A. Schweiger, L. Braunschweiler, J. Forrer, R. R. Ernst, *J. Magn. Reson.* **1986**, *66*, 74–85.
- [62] J. Peisach, W. B. Mims, J. L. Davis, *J. Biol. Chem.* **1979**, *254*, 2379–2389.
- [63] W. B. Mims, *Phys. Rev. B* **1972**, *5*, 2409–2419.
- [64] J. E. Wertz, J. R. Bolton, *Electron Spin Resonance; Elementary Theory and Practical Applications*, McGraw-Hill, New York, **1972**.
- [65] E. A. C. Lucken, *Nuclear quadrupole coupling constants*, Academic Press, London, **1969**.
- [66] W. B. Mims, *Phys. Rev. B* **1972**, *6*, 3543–3545.
- [67] A. Schweiger, G. Jeschke, *Principles of Pulse Electron Paramagnetic Resonance*, Oxford University Press, Oxford, UK, New York, **2001**.
- [68] S. Stoll, A. Schweiger, *J. Magn. Reson.* **2003**, *163*, 248–256.
- [69] E. J. Reijerse, A. M. Tyryshkin, S. A. Dikanov, *J. Magn. Reson.* **1998**, *131*, 295–309.
- [70] S. A. Dikanov, A. A. Shubin, V. N. Parmon, *J. Magn. Reson.* **1981**, *42*, 474–487.
- [71] D. Baute, D. Arieli, F. Neese, H. Zimmermann, B. M. Weckhuysen, D. Goldfarb, *J. Am. Chem. Soc.* **2004**, *126*, 11733–11745.

Received: April 15, 2013

Published online on September 6, 2013